Inorg. Chem. **2008**, *47*, 3540−3548

Inorganic Chemistry
Article

Steric Influence on the Excited-State Lifetimes of Ruthenium Complexes with Bipyridyl−Alkanylene−Pyridyl Ligands

Maria Abrahamsson,[†,‡] Maria J. Lundqvist,[§] Henriette Wolpher,[⊥] Olof Johansson,[†,⊥] Lars Eriksson,[||] Jonas Bergquist,[¶] Torben Rasmussen,[⊗] Hans-Christian Becker,[†] Leif Hammarström,[†] Per-Ola Norrby,[○] Björn Åkermark,[*,⊥] and Petter Persson[*,§,#]

Department of Photochemistry and Molecular Science, Uppsala University, Box 523, SE-751 20 Uppsala, Sweden, Department of Quantum Chemistry, Uppsala University, Box 518, SE-751 20 Uppsala, Sweden, Department of Organic Chemistry, Arrhenius Laboratory, Stockholm University, SE-106 91 Stockholm, Sweden, Division of Structural Chemistry, Stockholm University, SE-106 91 Stockholm, Sweden, Department of Analytical Chemistry, Uppsala University, Box 599, SE-751 24 Uppsala, Sweden, Department of Biochemistry and Organic Chemistry, Uppsala University, Box 576, SE-751 23 Uppsala, Sweden, Department of Chemistry, University of Gothenburg, Kemigården 4, SE-412 96 Göteborg, Sweden, and Department of Chemical Physics, Lund University, Box 124, SE-221 00 Lund, Sweden

Received October 1, 2007

The structural effect on the metal-to-ligand charge transfer (MLCT) excited-state lifetime has been investigated in bis-tridentate Ru(II)−polypyridyl complexes based on the terpyridine-like ligands [6-(2,2′-bipyridyl)](2-pyridyl)methane (**1**) and 2-[6-(2,2′-bipyridyl)]-2-(2-pyridyl)propane (**2**). A homoleptic ($[Ru(\mathbf{2})_2]^{2+}$) and a heteroleptic complex ($[Ru(ttpy)(\mathbf{2})]^{2+}$) based on the new ligand **2** have been prepared and their photophysical and structural properties studied experimentally and theoretically and compared to the results for the previously reported $[Ru(\mathbf{1})_2]^{2+}$. The excited-state lifetime of the homoleptic Ru^{II} complex with the isopropylene-bridged ligand **2** was found to be 50 times shorter than that of the corresponding homoleptic Ru^{II} complex of ligand **1**, containing a methylene bridge. A comparison of the ground-state geometries of the two homoleptic complexes shows that steric interactions involving the isopropylene bridges make the coordination to the central Ru^{II} ion less octahedral in $[Ru(\mathbf{2})_2]^{2+}$ than in $[Ru(\mathbf{1})_2]^{2+}$. Calculations indicate that the structural differences in these complexes influence their ligand field splittings as well as the relative stabilities of the triplet metal-to-ligand charge transfer (^{3}MLCT) and metal-centered (^{3}MC) excited states. The large difference in measured excited-state lifetimes for the two homoleptic Ru^{II} complexes is attributed to a strong influence of steric interactions on the ligand field strength, which in turn affects the activation barriers for thermal conversion from ^{3}MLCT states to short-lived ^{3}MC states.

Introduction

Ruthenium polypyridyl complexes have been extensively used as photoactive components in devices for solar energy conversion and molecular electronics, as well as for the study of light-induced charge separation in general.[1–3] In the preparation of donor−sensitizer−acceptor triads, bis-tridentate complexes are of special interest because the formation of rodlike molecular arrays is possible, allowing for vectorial electron transfer.[4] This is in contrast to the case for the widely used $[Ru(bpy)_3]^{2+}$ (bpy is 2,2′-bipyridine) type complexes,

* To whom correspondence should be addressed. E-mail: bjorn.akermark@organ.su.se (B.Å.); petter.persson@chemphys.lu.se (P.P.).
† Department of Photochemistry and Molecular Science, Uppsala University.
‡ Present address: Department of Chemistry, Johns Hopkins University, Baltimore, MD 21218.
§ Department of Quantum Chemistry, Uppsala University.
⊥ Department of Organic Chemistry, Stockholm University.
|| Department of Structural Chemistry, Stockholm University.
¶ Department of Analytical Chemistry, Uppsala University.
⊗ Department of Biochemistry and Organic Chemistry, Uppsala University.
○ Department of Chemistry, University of Gothenburg.
Department of Chemical Physics, Lund University.

(1) Kalyanasundaram, K. *Photochemistry of Polypyridine and Porphyrin Complexes*; Academic Press: London, 1992.
(2) Scandola, F.; Chiorboli, C.; Indelli, M. T.; Rampi, M. A. In *Electron Transfer in Chemistry*; Balzani, V., Ed.; Wiley-VCH: Weinheim, Germany, 2001; Vol. III.
(3) Barigelletti, F.; Flamigni, L. *Chem. Soc. Rev.* **2000**, *29*, 1.
(4) Sauvage, J.-P.; Collin, J.-P.; Chambron, J.-C.; Guillerez, S.; Coudret, C.; Balzani, V.; Barigelletti, F.; De Cola, L.; Flamigni, L. *Chem. Rev.* **1994**, *94*, 993.

10.1021/ic7019457 CCC: $40.75

Published on Web 04/11/2008

Scheme 1. Synthesis of Ligand **2**

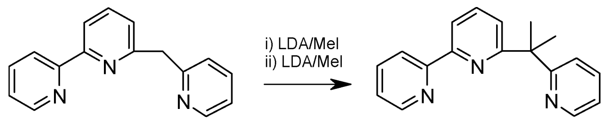

1 **2**

which upon functionalization with donor and acceptor moieties give rise to different geometrical isomers which may result in complicated kinetics. However, the excited-state lifetimes of homoleptic ruthenium(II)–bis-tridentate type complexes, such as $[Ru(tpy)_2]^{2+}$ (tpy is 2,2′:6′,2″-terpyridine), are generally about 3 orders of magnitude shorter than those of the corresponding bipyridine complexes.[4] The lowest triplet metal-to-ligand charge transfer (^{3}MLCT) excited state is rapidly converted, by thermal activation, to a short-lived triplet metal-centered (^{3}MC) state from which no photochemistry occurs.[1,5] The rapid ^{3}MLCT → ^{3}MC conversion is believed to be caused by the bite angles in terpyridine complexes, which are unfavorable for the formation of ideal octahedral complexes.[1,6,7] Terpyridines therefore fail to destabilize the lowest unoccupied metal d orbital relative to the lowest unoccupied ligand-centered orbital, and this is likely to influence the relative stabilities of the ^{3}MLCT and ^{3}MC excited states.

By preparation of terpyridine-like ligands consisting of a bipyridine coupled to a pyridine by a methylene group (ligand **1** in Scheme 1), complexes with a larger bite angle can be obtained.[8] This allows for a more octahedral structure and thus a higher energy for the ^{3}MC state, in turn resulting in a longer excited-state lifetime. It should be noted that there are several other possibilities for extending the excited-state lifetime of bis-tridentate Ru^{II} complexes, but most of these result in a reduced excited-state energy compared to that of $[Ru(bpy)_3]^{2+}$.[9] Since a low excited-state energy results in less driving force for vectorial electron and energy transfer processes, our approach is an interesting alternative for many applications. The complex $[Ru(\mathbf{1})_2]^{2+}$, where **1** is [6-(2,2′-bipyridyl)]-(2-pyridyl)methane (Figure 1), is the simplest example of a homoleptic complex based on this approach, and its excited-state lifetime is about 2 orders of magnitude longer than that of the parent bis-terpyridine complex.[8] By turning to an all-6-chelate-ring bis-tridentate complex, $[Ru(dqp)_2]^{2+}$ (dqp is 2,6-di(8-quinolinyl)pyridine), a room-temperature excited-state lifetime as long as 3 μs was recently obtained.[10] This is the longest lifetime reported for a Ru^{II} polypyridyl-type complex.

Homoleptic and heteroleptic complexes related to $[Ru(\mathbf{1})_2]^{2+}$ containing ligands with a keto, 1-hydroxyethane, or a 1-methoxyethane bridge have also recently been prepared and investigated.[11] It was observed that these modifications on the methylene bridge influence both the stability and emission lifetime negatively in comparison to $[Ru(\mathbf{1})_2]^{2+}$ and that the different substituents result in different electronic properties of the complexes.[11] However, the *gem*-dialkyl effect has been widely used in organic chemistry to explain the positive effect of geminal dialkyl substitution on methylene groups on the rates of cyclization and the stabilities of cyclic structures relative to open ones.[12] In a few early studies, the effect has been used to explain the stabilization of transition-metal complexes of bidentate ligands[13] and recently also the steric effects on phosphine ligands in reductive elimination from Pt^{IV} complexes.[14] It therefore seemed interesting to see if the *gem*-dialkyl effect could also serve to stabilize complexes related to $[Ru(\mathbf{1})_2]^{2+}$.

To further study the effects of ligand alterations, the related ligand 2-[6-(2,2′-bipyridyl)]-2-(2-pyridyl)propane (**2**) (Scheme 1) and the corresponding homoleptic complex $[Ru(\mathbf{2})_2]^{2+}$ and the heteroleptic complex $[Ru(ttpy)(\mathbf{2})]^{2+}$ (ttpy is 4′-tolyl-2,2′:6′,2″-terpyridine) have been prepared (Figure 1). The new ligand **2** and its Ru^{II} complexes were selected for this study in order to minimize the difference in electronic properties of the ligands compared to those of the corresponding complexes with ligand **1**. This makes it possible to focus on purely structural effects on the photophysical properties more directly than could previously be achieved with the ligands containing hydroxyl or methoxy groups. New complexes with ligand **2** have been investigated with spectroscopic and electrochemical techniques to measure structural and photophysical properties. Since the *gem*-dialkyl effect has its origin in conformational factors, molecular mechanics structure analysis was performed on the homoleptic complex $[Ru(\mathbf{2})_2]^{2+}$. In order to understand the differences in photophysics of $[Ru(\mathbf{1})_2]^{2+}$ and $[Ru(\mathbf{2})_2]^{2+}$, quantum chemical calculations were performed of both ground and excited-state properties.

Results and Discussion

Synthesis. The syntheses of ligand **1** and the corresponding complexes have been described elsewehere.[8,11] Ligand **2** was synthesized by methylation of the methylene group in ligand **1** (Scheme 1). The homoleptic complex $[Ru(\mathbf{2})_2]^{2+}$ and the heteroleptic complex $[Ru(ttpy)(\mathbf{2})]^{2+}$ (Figure 1) were prepared by standard procedures and characterized by NMR and ESI-FTICR-MS, which were in accordance with the assigned structures.

Ground-State Structural Properties. The crystal structure of $[Ru(\mathbf{2})_2]^{2+}$ shows that this complex is less octahedral

(5) Meyer, T. J. *Pure Appl. Chem.* **1986**, *58*, 1193.
(6) Thummel, R. P.; Jahng, Y. *Inorg. Chem.* **1986**, *25*, 2527.
(7) Calvert, J. M.; Caspar, J. V.; Binstead, R. A.; Westmoreland, T. D.; Meyer, T. J. *J. Am. Chem. Soc.* **1982**, *104*, 6620.
(8) Wolpher, H.; Johansson, O.; Abrahamsson, M.; Kritikos, M.; Sun, L.; Åkermark, B. *Inorg. Chem. Commun.* **2004**, *7*, 337.
(9) Medlycott, E. A.; Hanan, G. S. *Chem. Soc. Rev.* **2005**, *34*, 133.
(10) Abrahamsson, M.; Jäger, M.; Österman, T.; Eriksson, L.; Persson, P.; Becker, H.-C.; Johansson, O.; Hammarström, L. *J. Am. Chem. Soc.* **2006**, *128*, 12616.
(11) Abrahamsson, M.; Wolpher, H.; Johansson, O.; Larsson, J.; Kritikos, M.; Eriksson, L.; Norrby, P.-O.; Bergquist, J.; Sun, L.; Åkermark, B.; Hammarström, L. *Inorg. Chem.* **2005**, *44*, 3215.
(12) (a) Beesley, R. M.; Ingold, C. K.; Thorpe, J. F. *J. Chem. Soc.* **1915**, *107*, 1080. (b) Parrill, A. L.; Dolata, D. P. *J. Mol. Struct. (THEOCHEM)* **1996**, *370*, 187. (c) Jung, M. E.; Piizzi, G. *Chem. Rev.* **2005**, *105*, 1735.
(13) (a) Shaw, B. L. *Adv. Chem. Ser.* **1982**, *196*, 101. (b) Hares, G. B.; Fernelius, C.; Douglas, B. D. *J. Am. Chem. Soc.* **1956**, *78*, 1816.
(14) (a) Marcone, J. E.; Moloy, K. G. *J. Am. Chem. Soc.* **1998**, *120*, 8527. (b) Arthur, K. L.; Wang, Q. L.; Bregel, D. M.; Smythe, N. A.; O'Neill, B. A.; Golberg, K. I.; Moloy, K. G. *Organometallics* **2005**, *24*, 4624.

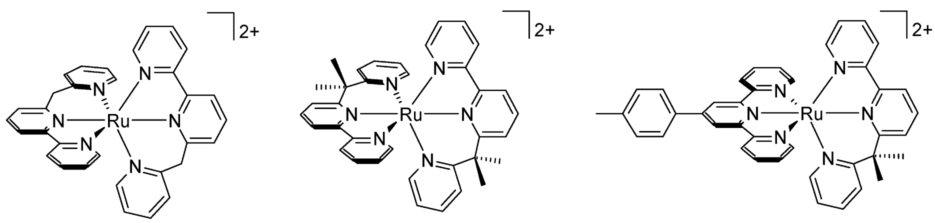

$[Ru(\mathbf{1})_2]^{2+}$ $[Ru(\mathbf{2})_2]^{2+}$ $[Ru(ttpy)(\mathbf{2})]^{2+}$

Figure 1. Complexes discussed in this paper.

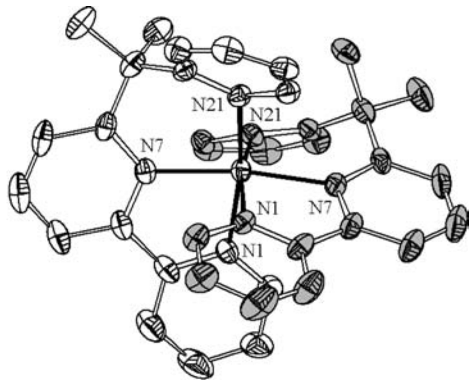

Figure 2. Crystal structure of $[Ru(\mathbf{2})_2]^{2+}$. Hydrogens are omitted for clarity. Ellipsoids are shown at the 30% probability level.

Table 1. Selected Crystal Data for $[Ru(\mathbf{2})_2]^{2+}$

empirical formula	$C_{36}H_{34}F_{12}N_6P_2Ru$
temp, K	293(2)
fw	941.70
cryst syst	trigonal
space group	$P\bar{3}1c$
a, Å	24.4440(4)
c, Å	12.4660(4)
V, Å^3	6450.6(3)
Z	6
ρ_{calcd}, g cm^{-3}	1.454
μ (Mo Kα), (mm^{-1})	0.524
cryst shape	plate
N (measd), N (unique), R (int)	52179, 4394, 0.0479
N (obsd), N (param), S (GOF)	3841, 265, 1.324
R1, wR2 ($I > 2\sigma(I)$)	0.0657, 0.0843
R1, wR2 (all data)	0.0888, 0.0887
$\Delta\rho_{min}$, $\Delta\rho_{max}$ (e/Å^3)	−0.275, +0.400

than $[Ru(\mathbf{1})_2]^{2+}$ (Figure 2). Selected crystal data are given in Table 1, and the N−Ru−N angles and Ru−N distances are given in Table 2. The Ru−N(bpy) distances in $[Ru(\mathbf{2})_2]^{2+}$ are 2.041–2.067 Å, and the Ru−N(py) distances are 2.143 Å, which are close to the corresponding distances in $[Ru(\mathbf{1})_2]^{2+}$. The ligand bite angles are N1−Ru−N21 = 165.16°, and N7−Ru−N7′ = 170.61°, with the primes denoting nitrogen atoms on the second ligand. This situation is less favorable than in $[Ru(\mathbf{1})_2]^{2+}$, where the corresponding angles (168.4 and 178.8°) are closer to an octahedral structure. Still, $[Ru(\mathbf{2})_2]^{2+}$ has a coordination more octahedral than that of $[Ru(tpy)_2]^{2+}$ (the X-ray structure shows bite angles of 158.4−159.1 and 178.8°, respectively).[15]

One rather large difference between the structures of $[Ru(\mathbf{2})_2]^{2+}$ and $[Ru(\mathbf{1})_2]^{2+}$ is the N−Ru−N angles between the lone pyridines. In $[Ru(\mathbf{2})_2]^{2+}$ this angle is 109.74°, while the corresponding angle in $[Ru(\mathbf{1})_2]^{2+}$ is only 98.9°. The bent structure of the coordinated ligand **2** forces the pyridines away from each other. In addition, the crystal structure reveals that the lone pyridines are tilted out of the plane of the bipyridine part. The dihedral angle in $[Ru(\mathbf{2})_2]^{2+}$ is around 60°, which can be compared to the recently published almost octahedral $[Ru(dqp)_2]^{2+}$ complex, with dihedral angles of about 35 and 39°.[10] The observed structural differences are most likely governed by steric effects within the complexes, although packing forces in the crystal is another possible explanation.

To gain a further understanding of the structural differences between $[Ru(\mathbf{1})_2]^{2+}$ and $[Ru(\mathbf{2})_2]^{2+}$, a computational study was performed, combining molecular mechanics (MM) and quantum chemical calculations. Initially, a MM conformational search on the homoleptic complex $[Ru(\mathbf{2})_2]^{2+}$ revealed several low-energy conformations with a global minimum, **MM-1**, even closer to octahedral than the structure of $[Ru(\mathbf{1})_2]^{2+}$. Key structural parameters of the three lowest energy conformations are given in Table 2. The X-ray crystal structure corresponds to the third lowest energy conformation, **MM-3,** which is only 5.5 kJ/mol above the global minimum, **MM-1**. Density functional theory (DFT) geometry optimizations, using the three MM structures as starting geometries, resulted in two unique structures, **a** and **b** (Figure 3), one from the third lowest energy MM conformer (**a**) and one from the two lowest energy MM conformers (**b**). According to the DFT calculations, however, **a** is 26 kJ/mol more stable than **b**, in qualitative contrast to the MM result. The isopropylene moiety is oriented differently relative to the bipyridine and pyridine planes in the two DFT geometries (see Figure 3). The higher energy conformer **b** has a more planar ligand orientation and, thus, a more octahedral configuration (see bond angles in Table 2 and Figure 3). However, the strain imposed on the system makes **b** substantially less stable. In the more stable conformer **a**, the pyridine and bipyridine moieties are bent out of plane, which makes the ruthenium surroundings less octahedral. By comparison of the computationally and experimentally determined N−Ru−N angles (Table 2), it can be seen that the lowest energy conformer from DFT matches the crystal structure very well. This supports the conclusion that the distorted structure originates from steric interactions involving the isopropylene bridges.

The Ru−N bond distances of the DFT structures are summarized in Table 2. All bond distances are highly similar and are within 0.01 Å, except for the Ru−N(py) distance, which is 0.05 Å shorter for the less stable complex **b**. The employed computational method is known to slightly over-

(15) Lashgari, K.; Kritikos, M.; Norrestam, R.; Norrby, T. *Acta Crystallogr., Sect. C* **1999**, *C55*, 64.

Table 2. N−Ru−N Angles (deg) and Ru−N Distances (Å) in the Crystal, MM, and DFT Structures of $[Ru(\mathbf{2})_2]^{2+}$ [a]

	cryst	MM-1	MM-2	MM-3	DFTa	DFTb
N1−Ru−N21	165.16(9)	171.1	171.4	169.3	165.5	173.4
N7−Ru−N7′	170.61(13)	173.0	170.5	169.8	170.3	169.1
N1−Ru−N7	80.43(9); 92.67(9)	80.0	80.1	80.0	80.1	80.6
N7−Ru−N21	90.27(9); 95.14(9)	91.4	91.7	92.3	89.6	93.0
N21−Ru−N21′	109.74(12)	89.3	93.9	101.8	108.0	88.6
Ru−N1	2.041(2)	2.052	2.054	2.057	2.086	2.087
Ru−N7	2.067(2)	2.044	2.046	2.058	2.097	2.089
Ru−N21	2.143(2)	2.062	2.064	2.087	2.182	2.132

[a] Atom numbering is given according to Figure 2, with the nitrogen atoms on the second ligand marked with primes.

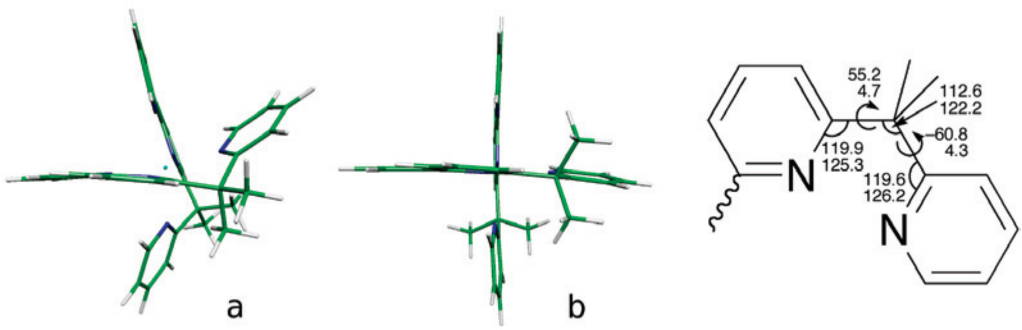

Figure 3. Views along the bipyridine planes of the two geometry-optimized DFT conformers of $[Ru(\mathbf{2})_2]^{2+}$ (left and center), where **a** is the most stable conformer and angles and dihedral angles (deg) around the isopropylene bridge of the **a** (upper values) and **b** (lower values) conformers (right).

Table 3. Electrochemical and Photophysical Data[a]

complex	absorption[b] λ_{max} (nm) ($\epsilon \times 10^{-4}$)	emission[c] (298 K) λ_{max} (nm)	emission[c] (298 K) τ (ns)	emission[c] (298 K) Φ	emission[c] (77 K) λ_{max} (nm)	emission[c] (77 K) τ (μs)	emission[c] (77 K) Φ	$E_{1/2}$, V[d] $Ru^{3+/2+}$	$E_{1/2}$, V[d] $Ru^{2+/+}$ [e]
$[Ru(\mathbf{2})_2]^{2+}$	472 (0.74)	650	0.3	1×10^{-4}	603	3.5	0.52	0.84	−1.64
$[Ru(ttpy)(\mathbf{2})]^{2+}$	485 (1.5)	[f]	∼0.1	$<2 \times 10^{-5}$	650	5.6	0.44	0.82	−1.58
$[Ru(\mathbf{1})_2]^{2+}$ [g]	477 (0.82)	655	15.0	1×10^{-3}	609	3.7	0.21	0.78	−1.67
$[Ru(tpy)_2]^{2+}$ [h]	476 (1.8)	[i]	0.25	[i]	598	11.0[j]	0.48[j]	0.91[k]	−1.62[k]
$[Ru(ttpy)_2]^{2+}$ [h]	490 (2.8)	640	0.95	3.2×10^{-5}	628	12.3[j]	0.45[j]	0.86[k]	−1.62[k]
$[Ru(bpy)_3]^{2+}$	450 (1.4)[j]	630[j]	1150[j]	0.089[j]	582[j]	5.1[j]	0.38[j]	0.88	−1.74

[a] All complexes are $[PF_6]^-$ salts. [b] In CH_3CN solution. [c] In a methanol:ethanol mixture (1:4, v/v). [d] In CH_3CN−0.1 M $(n\text{-}C_4H_9)_4N(PF_6)$ vs $Fc^{+/0}$; $\upsilon = 0.1$ V s^{-1}. [e] Ligand-centered reduction. [f] Very weak emission centered around 650–700 nm. [g] From ref 11. [h] From ref 4. [i] Not given. [j] From ref 19. [k] Data recalculated from literature values in ref 4 vs SSCE by subtracting 0.385 V.

estimate Ru−N distances,[16–18] and this is confirmed also for the present system when comparing the calculated Ru−N distances with the crystal structure values. The calculated Ru−N(bpy) distances of 2.09–2.10 Å are all longer than the experimental distances of 2.04–2.07 Å. The Ru−N(py) distances are 2.13 and 2.18 Å with DFT and 2.14 Å in the crystal structure. A good agreement between the DFT calculations and the experimental structure determination of this complex was thus obtained, in terms of the correct theoretical prediction of which conformer is the most stable, as well as the accuracy of its calculated structural properties. This is reassuring for the appropriateness of the computational methodology to investigate these types of Ru^{II} complexes.

Electrochemical Properties. The redox properties of the new complexes were investigated by cyclic voltammetry in acetonitrile and are very similar to those of the corresponding complexes based on ligand **1**. Thus, cyclic voltammetry (see Table 3) of $[Ru(\mathbf{2})_2]^{2+}$ showed a reversible one-electron $Ru^{III/II}$ oxidation at 0.84 V vs $Fc^{+/0}$ and a reversible one-electron ligand reduction at −1.64 V. The corresponding oxidation and reductions in $[Ru(ttpy)(\mathbf{2})]^{2+}$ were found at 0.82 and −1.58 V, respectively. This is also very similar to the properties of the parent $[Ru(tpy)_2]^{2+}$ complex.[4] Nevertheless, it is clear that the first reduction in $[Ru(ttpy)(\mathbf{2})]^{2+}$ is localized on the ttpy ligand, as the tpy and ttpy complexes consistently show potentials of reduction less negative than those of the homoleptic $[Ru(\mathbf{1})_2]^{2+}$ and $[Ru(\mathbf{2})_2]^{2+}$.

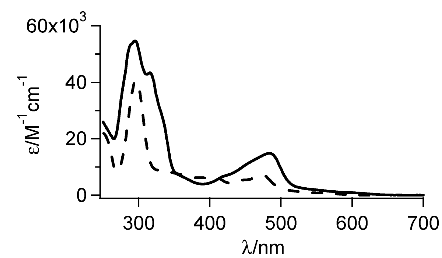

Figure 4. UV–vis electronic spectra for $[Ru(\mathbf{2})_2]^{2+}$ (dashed line) and $[Ru(ttpy)(\mathbf{2})]^{2+}$ (solid line) in acetonitrile solution.

Electronic Absorption Spectra. The UV–vis spectra of the complexes in acetonitrile are shown in Figure 4, and absorption maxima and molar absorption coefficients are found in Table 3. Both $[Ru(\mathbf{2})_2]^{2+}$ and $[Ru(ttpy)(\mathbf{2})]^{2+}$ show

(16) Gorelsky, S. I.; Lever, A. B. P. *J. Organomet. Chem.* **2001**, *635*, 187.
(17) Zhou, X.; Ren, A. M.; Feng, J. K. *J. Organomet. Chem.* **2005**, *690*, 338.
(18) Zheng, K. C.; Wang, J. P.; Peng, W. L.; Liu, X. W.; Yun, F. C. *J. Mol. Struct. (THEOCHEM)* **2002**, *582*, 1.

spectral features similar to those of the related complexes based on bpy-py ligands[8,11] with normal singlet MLCT (^{1}MLCT) absorption bands in the region above 400 nm and ligand-based transitions around 300 nm. The homoleptic complex has its maximum at 472 nm, while the heteroleptic complex has its highest absorption at 485 nm. The ^{1}MLCT band is twice as strong in the heteroleptic complex due to the ttpy ligand.[11] In the UV region the heteroleptic complex shows the two expected ligand-based absorption peaks at around 294 and 319 nm (corresponding to the different ligands), while the homoleptic complex shows an absorption band centered around 297 nm. $[Ru(\mathbf{2})_2]^{2+}$ also shows an additional feature just below 400 nm, which may be attributed to higher energy MLCT transitions involving mainly pyridine-based π^* orbitals. A similar feature below 400 nm is also found in the spectrum of $[Ru(\mathbf{1})_2]^{2+}$.

According to time-dependent DFT (TD-DFT) calculations of excitations from the ground state of $[Ru(\mathbf{1})_2]^{2+}$ and $[Ru(\mathbf{2})_2]^{2+}$ (conformer **a**), there are d $\rightarrow \pi^*$ (bpy) transitions above 400 nm and intraligand transitions below 315 nm (see Table S1 in the Supporting Information). Additionally, there are several weak transitions in the 320–400 nm region of the calculated spectra which mainly consist of d $\rightarrow \pi^*$ (bpy) transitions mixed with minor d $\rightarrow$ d contributions.

Steady-State Emission Properties. Steady-state emission properties of $[Ru(\mathbf{2})_2]^{2+}$ and $[Ru(ttpy)(\mathbf{2})]^{2+}$ are summarized in Table 3. Both complexes emit very weakly at room temperature. $[Ru(\mathbf{2})_2]^{2+}$ displays an emission maximum at 650 nm, while the corresponding heteroleptic complex emits so weakly that it is impossible to determine the position of the maximum. Consequently, emission quantum yields are very low at room temperature. Low-temperature (77 K) emission quantum yields are comparable to those for the parent $[Ru(bpy)_3]^{2+}$ and $[Ru(tpy)_2]^{2+}$ complexes, indicating that the complexes behave as bis-tridentate Ru^{II}−polypyridyl complexes in general.[19] Furthermore, as reported in Table 3, the highest energy emission peaks of $[Ru(\mathbf{2})_2]^{2+}$ and $[Ru(ttpy)(\mathbf{2})]^{2+}$ at 77 K are found at 603 and 650 nm, respectively. Taking these values as measures of the excited-state energies[20] of the two complexes, this shows that $[Ru(\mathbf{2})_2]^{2+}$ has almost maintained the energy of the parent $[Ru(tpy)_2]^{2+}$ complex, while the heteroleptic complex is significantly red-shifted. This trend is also similar to what is seen when $[Ru(\mathbf{1})_2]^{2+}$ is compared with its corresponding heteroleptic complex $[Ru(ttpy)(\mathbf{1})]^{2+}$, which have emission maxima at 77 K at 609 and 637 nm, respectively.

By visual inspection of the 77 K spectra (Figure 5), it can be seen that the geometrical distortion between the ground and excited states is larger in the heteroleptic complex than in the corresponding homoleptic species, as judged from the intensity ratio of the first and second vibrational peaks and loss of vibronic structure.[5] This is somewhat surprising, since this distortion typically is smaller for a ^{3}MLCT state localized on a ttpy ligand (expected for $[Ru(ttpy)(\mathbf{2})]^{2+}$ on the basis of electrochemistry data), compared to a bpy ligand. This is also in contrast to the results for the related complexes discussed previously.[11] The two homoleptic complexes $[Ru(\mathbf{2})_2]^{2+}$ and $[Ru(\mathbf{1})_2]^{2+}$ display almost the same intensity ratio.

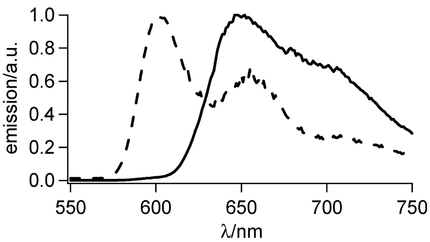

Figure 5. Corrected and normalized steady-state emission spectra at 77 K for $[Ru(\mathbf{2})_2]^{2+}$ (dashed line) and $[Ru(ttpy)(\mathbf{2})]^{2+}$ (solid line) in MeOH:EtOH (1:4).

Time-Resolved Emission Properties. Time-resolved emission properties of $[Ru(\mathbf{2})_2]^{2+}$ and $[Ru(ttpy)(\mathbf{2})]^{2+}$ are summarized in Table 3. The excited-state lifetimes at room temperature are around 0.1 and 0.3 ns for $[Ru(ttpy)(\mathbf{2})]^{2+}$ and $[Ru(\mathbf{2})_2]^{2+}$, respectively. These values are similar to the 0.25 ns excited-state lifetime of the reference complex $[Ru(tpy)_2]^{2+}$ and are significantly shorter than the 15 ns excited-state lifetime of $[Ru(\mathbf{1})_2]^{2+}$. In frozen matrices, however, both complexes display excited-state lifetimes in the microsecond region. This is expected, since the thermally activated nonradiative decay via ^{3}MC states is insignificant at liquid-nitrogen temperature.

It is striking that $[Ru(\mathbf{2})_2]^{2+}$ has an excited-state lifetime at room temperature that is approximately 50 times shorter compared to that of $[Ru(\mathbf{1})_2]^{2+}$, although the only structural difference between these two complexes is the presence of the methyl side groups in $[Ru(\mathbf{2})_2]^{2+}$. The side groups in $[Ru(\mathbf{2})_2]^{2+}$ are not expected to contribute directly to the frontier molecular orbitals. It is therefore reasonable to assume that they primarily influence the photophysical properties via steric effects which cause $[Ru(\mathbf{2})_2]^{2+}$ to be significantly more distorted from an ideal octahedral coordination than that of $[Ru(\mathbf{1})_2]^{2+}$. Such a structural distortion can be expected to modify the ligand field splitting of the central metal ion in such a way that the ^{3}MC states are stabilized, leading to a more rapid activated decay via those states. This is analyzed in greater detail below using quantum chemical calculations.

Calculated Excited-State Properties. In order to provide a detailed explanation for the large difference in observed excited-state lifetimes between $[Ru(\mathbf{1})_2]^{2+}$ and $[Ru(\mathbf{2})_2]^{2+}$, additional DFT and TD-DFT calculations were performed on these two complexes. In addition to the ground-state (S_0) geometries described above, the lowest ^{3}MLCT and ^{3}MC states of the two complexes were located using unrestricted triplet optimizations. The lowest ^{3}MLCT states of the two complexes were found by performing an unrestricted triplet optimization starting from the optimized ground-state geometry. To locate the ^{3}MC states, the structures were

(19) Juris, A.; Balzani, V.; Barigelletti, F.; Campagna, S.; Belser, P.; von Zelewsky, A. *Coord. Chem. Rev.* **1988**, *84*, 85.
(20) (a) Treadway, J.; Loeb, B.; Lopez, R.; Anderson, P. A.; Keene, F. R.; Meyer, T. J. *Inorg. Chem.* **1996**, *35*, 2242. (b) Hammarström, L.; Barigelletti, F.; Flamigni, L.; Indelli, M. T.; Armaroli, N.; Calogero, G.; Guardigli, M.; Sour, A.; Collin, J.-P.; Sauvage, J.-P. *J. Phys. Chem. A* **1997**, *101*, 9061. (c) Caspar, J. V.; Meyer, T. J. *Inorg. Chem.* **1983**, *22*, 2444.

Table 4. Selected Ru−N Bond Lengths in the Three Investigated States S_0, ^{3}MLCT, and ^{3}MC and the Nuclear Coordinate[a] (in Å)

	$[Ru(\mathbf{1})_2]^{2+}$			$[Ru(\mathbf{2})_2]^{2+}$		
	S_0	^{3}MLCT	^{3}MC	S_0	^{3}MLCT	^{3}MC
Ru−N21 (py *xy*)[b]	2.15	2.15	2.26	2.18	2.17	2.27
Ru−N7 (bpy *z* axis)[b]	2.08	2.07	2.10	2.10	2.09	2.13
Ru−N1 (bpy *xy*)[b]	2.10	2.08	2.34	2.09	2.07	2.31
nuclear coordinate[a]	0	–0.060	0.752	0	–0.059	0.690

[a] Obtained as the sum of the geometrical change (in Å) of the six Ru−N distances relative to the ground-state geometry. [b] Atom numbering according to Figure 2.

distorted in order to get a good starting guess for a subsequent unrestricted triplet optimization. The philosophy used for construction of a starting structure for ^{3}MC state optimization was rather simple. A more octahedral coordination of pyridyl ligands will increase the energy of the unoccupied d orbitals (d_{z^2} and $d_{x^2-y^2}$), since their lobes will point directly toward the nitrogen lone pairs. Similarly, displacing the pyridyl ligands away from the ruthenium core will lower the energy of the unoccupied d-orbitals, to a point where one of them (d_{z^2} or $d_{x^2-y^2}$) becomes occupied. Therefore, the starting structures were constructed by elongation of the Ru−N bonds in the *xy* plane and thus populating the $d_{x^2-y^2}$ orbital, which is the unoccupied d orbital lowest in energy in the ground-state electronic structures of $[Ru(\mathbf{1})_2]^{2+}$ and $[Ru(\mathbf{2})_2]^{2+}$. The calculated Ru−N bonds of the resulting singlet- and triplet-state geometries are listed in Table 4.

For both systems, the distortion of the geometry from the S_0 to the ^{3}MLCT state is small and the Ru−N bonds for the triplet are slightly shorter than for the singlet. The geometric displacements from the S_0 to the ^{3}MC state, on the other hand, are relatively large and the Ru−N bonds are longer by 0.02–0.24 Å in the ^{3}MC state. A clear elongation of the Ru−N bonds in the *xy* plane (Ru−N1 and Ru−N21) can be seen, which corresponds to population of the $d_{x^2-y^2}$ orbital. The largest geometric displacement is seen in the ^{3}MC state of $[Ru(\mathbf{1})_2]^{2+}$. Mulliken population analysis was used to characterize the nature of the triplet states. In the optimized ^{3}MLCT state of $[Ru(\mathbf{1})_2]^{2+}$, the net spin is 0.91 located at the Ru core and the remaining spin is distributed over the ligands (mainly on the bipyridyls), and the ^{3}MC state has a net spin of 1.81 located at Ru. For $[Ru(\mathbf{2})_2]^{2+}$, the net spins are 0.90 and 1.79 at the Ru core in the ^{3}MLCT and ^{3}MC states, respectively. These calculated Mulliken spin densities are thus, for both complexes, in qualitative agreement with the generally anticipated increase from one to two unpaired electrons localized on the central Ru ion accompanying a ^{3}MLCT to ^{3}MC transition.

For both complexes, the different natures of the triplet states at the ^{3}MLCT and ^{3}MC optimized geometries are clearly reflected in their molecular orbital (MO) structures. This is illustrated in Figure 6, where the highest occupied MO (α-HOMO) and lowest unoccupied MO (β-LUMO), obtained from the unrestricted triplet calculations, are shown for each of the two states for both complexes. In a simple one-electron picture, the change in electronic structure on going from the singlet ground state, S_0, to the lowest triplet state corresponds to taking one electron (with β spin) from a doubly occupied MO in S_0 and placing it (with α spin) in

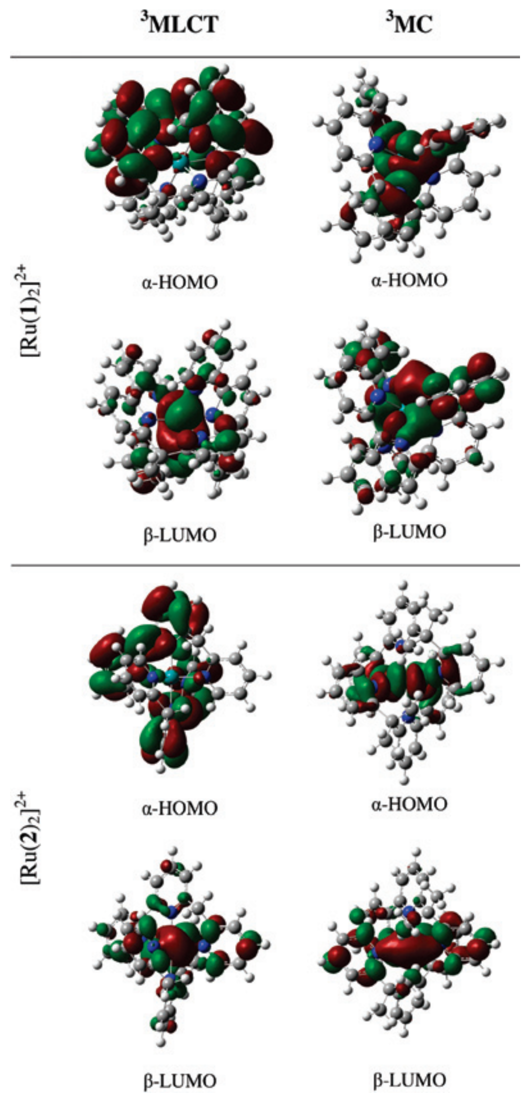

Figure 6. Calculated highest occupied molecular orbital (α-HOMO) and lowest unoccupied molecular orbital (β-LUMO) for the ^{3}MLCT and ^{3}MC states of $[Ru(\mathbf{1})_2]^{2+}$ and $[Ru(\mathbf{2})_2]^{2+}$ according to unrestricted triplet calculations at the respective optimized geometries.

the lowest unoccupied MO in S_0. Thus, the triplet β-LUMO loosely corresponds to the hole formed among the occupied MOs in S_0, and the triplet α-HOMO loosely corresponds to the additional electron among the unoccupied MOs in S_0. According to the β-LUMOs shown in Figure 6, an electron is removed from a Ru t_{2g} level for all investigated triplet states. For the ^{3}MLCT states of the two complexes, the α-HOMO corresponds to a ligand π* orbital, while for the ^{3}MC states of the two complexes, the main contributions to the α-HOMO comes from a Ru e_g orbital. These clear qualitative differences in the MO structures for both complexes thus agree with the assignments of the ^{3}MLCT and ^{3}MC states made above.

The relation between the structure and energetics of the two systems is illustrated by the calculated energy diagrams in Figure 7. The energy diagrams have been constructed from calculated Ru−N distances (nuclear coordinate), total energies of optimized states (gas-phase electronic energy of the S_0, ^{3}MLCT, and ^{3}MC states), singlet single-point energies at the triplet geometries, and vertical singlet and triplet

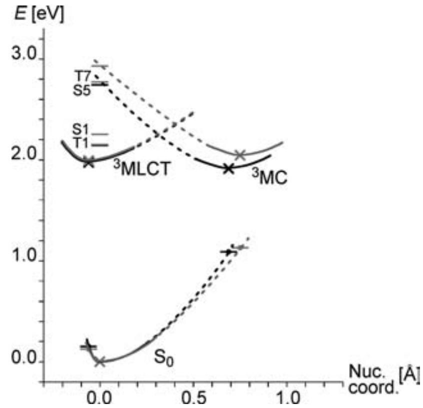

Figure 7. Calculated energy diagram of $[Ru(\mathbf{1})_2]^{2+}$ (gray) and $[Ru(\mathbf{2})_2]^{2+}$ (black). The total energies of the DFT optimized states, i.e. the S_0, ^{3}MLCT, and ^{3}MC states are denoted by crosses. Vertical single-point energies of the S_0 surface for the ^{3}MLCT and ^{3}MC geometries are indicated by dots on a horizontal bar. Vertical singlet and triplet excitation energies of the S_0 state are shown as horizontal bars and denoted as follows: T1 is the lowest vertical singlet–triplet transitions from S_0 to a ^{3}MLCT surface and T7 the lowest vertical singlet–triplet excitation from S_0 to a ^{3}MC surface. S1 is the lowest singlet–singlet transition of MLCT character, and S5 the lowest singlet–singlet transition of MLCT character with a significant oscillator strength.

TD-DFT excitation energies at the singlet geometries. The values of the nuclear coordinate (*x* axis in the diagram) were obtained as the sum of the geometrical change (in Å) of the six Ru−N distances relative to the ground-state geometry. All energy values are given relative to the singlet ground-state energy.

According to the calculations of vertical singlet excitations from the ground-state geometry, the absorptions in the two systems are highly similar. For both systems, the lowest singlet excitation (S1) is found at 2.25 eV, and the lowest MLCT excitation with significant oscillator strength is found in the fifth lowest excitation (S5) at 2.77 eV for $[Ru(\mathbf{1})_2]^{2+}$ and 2.74 eV for $[Ru(\mathbf{2})_2]^{2+}$.

The lowest ^{3}MLCT states are located at 1.99 and 1.97 eV compared to the S_0 state, where the ^{3}MLCT state of $[Ru(\mathbf{2})_2]^{2+}$ is the most stable one. These values correspond very well with the experimentally obtained excited-state energies of 2.04 and 2.06 eV obtained for the two complexes, respectively, from the 77 K emission maxima given in Table 3. The differences between the two complexes are, furthermore, essentially negligible for both the experiments and the calculations. Although there are several approximations in the calculations, such as the neglect of solvent effects, which could mean that the excellent quantitative agreement between experiment and theory is somewhat fortuitous, the good qualitative agreement gives confidence to the description of the photophysics in general and to the nature of the ^{3}MLCT state in particular.

As seen in Figure 7, there appears to be a more significant difference between the two complexes for the ^{3}MC states than for the ^{3}MLCT states. While the ^{3}MLCT states of the two complexes appear to have essentially identical excited-state energies, the ^{3}MC state of $[Ru(\mathbf{2})_2]^{2+}$ is calculated to be lower in energy than the ^{3}MC state of $[Ru(\mathbf{1})_2]^{2+}$. For $[Ru(\mathbf{1})_2]^{2+}$ the ^{3}MC state is 0.05 eV higher in energy compared to the ^{3}MLCT state. For $[Ru(\mathbf{2})_2]^{2+}$, however, the ^{3}MC state is the most stable triplet state: 0.06 eV more stable than the ^{3}MLCT state. In addition, the vertical distance to the ground-state surface is shorter for $[Ru(\mathbf{2})_2]^{2+}$. Also, the energy difference between vertical triplet excitations from S_0 to the lowest excitations that can be assigned to the ^{3}MLCT and ^{3}MC surfaces, T1 and T7 in Figure 7, respectively, indicate that the ^{3}MC surface is located higher in the case of $[Ru(\mathbf{1})_2]^{2+}$. These differences in vertical excitations are 0.78 eV for $[Ru(\mathbf{1})_2]^{2+}$ and 0.63 eV for $[Ru(\mathbf{2})_2]^{2+}$.

The activation barrier for ^{3}MLCT to ^{3}MC conversion has been estimated experimentally to be 0.37 eV for $[Ru(\mathbf{1})_2]^{2+}$.[11] The calculated difference in relative energies of the ^{3}MLCT and ^{3}MC states can, furthermore, be used to obtain a rough estimate of the difference between $[Ru(\mathbf{1})_2]^{2+}$ and $[Ru(\mathbf{2})_2]^{2+}$ in activation barrier for the ^{3}MLCT to ^{3}MC conversion. Using a simple Marcus-type interpolation, which determines that the difference in activation barrier is roughly half-the difference in reaction energy, a ca. 0.06 eV lower activation barrier is estimated for $[Ru(\mathbf{2})_2]^{2+}$. This would correspond to a significant lowering of the energy barrier that is qualitatively compatible with the experimental finding of a significantly shorter excited-state lifetime of $[Ru(\mathbf{2})_2]^{2+}$ compared to that for $[Ru(\mathbf{1})_2]^{2+}$. In addition, the difference in reorganization energy between $[Ru(\mathbf{1})_2]^{2+}$ and $[Ru(\mathbf{2})_2]^{2+}$ may also be of importance for the observed excited-state lifetime.

The calculations suggest that the main reason for the distinct shortening of the excited-state lifetime of $[Ru(\mathbf{2})_2]^{2+}$ compared to that of $[Ru(\mathbf{1})_2]^{2+}$ at room temperature is the steric influence of the isopropylene bridge in $[Ru(\mathbf{2})_2]^{2+}$ giving rise to a reduced ligand field splitting that lowers the equilibrium energy of the ^{3}MC state. In fact, the calculations even suggest that the ^{3}MC state potential energy surface minimum is situated below that of the ^{3}MLCT potential energy surface for $[Ru(\mathbf{2})_2]^{2+}$. This is an interesting finding, since the ^{3}MC state is usually believed to be higher in energy than the ^{3}MLCT state. The transition from ^{3}MLCT to ^{3}MC is often irreversible, due to very fast nonradiative decay back to the ground state from the metal-centered state. In such a case the activation barrier will correspond to the energy difference between the ^{3}MLCT equilibrium energy and the potential energy surface crossing point between the two states. However, if the ^{3}MC → ^{3}MLCT back-reaction is sufficiently fast to compete with the nonradiative decay of the ^{3}MC state to effectively establish an equilibrium between the ^{3}MLCT and ^{3}MC triplet states, the activation energy will correspond to the difference in equilibrium energies of the two states. Thus, the difference in activation barrier between $[Ru(\mathbf{1})_2]^{2+}$ and $[Ru(\mathbf{2})_2]^{2+}$ may reflect the same process in the two complexes, or two different processes.

It is noteworthy that the triplet-state calculations indicate that the triplet potential energy surfaces are rather flat and that the differences between the calculated properties of the two homoleptic Ru^{II} complexes are quite small. This means that some of the detailed conclusions drawn for these states should be regarded with some caution. Nevertheless, the qualitative agreement with the experimentally observed excited-state lifetimes suggests that the calculations correctly capture essential differences between the two complexes in terms of the influence of the steric effects on the excited-state properties.

Conclusions

A combination of experimental and theoretical techniques has been used to investigate the relationship between structure and photophysical properties of Ru^{II} bis-tridentate complexes containing bipyridyl−alkanylene−pyridyl ligands.

Structurally, the coordination to the Ru^{II} ion in a homoleptic complex containing polypyridyl ligands with bulky isopropylene bridges was found to be significantly distorted in comparison to that of the corresponding Ru^{II} complex with methylene bridges. DFT calculations were able to predict geometrical properties of the Ru^{II} complexes, as they reproduced X-ray crystal structures well. Differences between relative stabilities of structural minima for DFT and MM methods suggest that there is room for improvement of the MM parameters. Even without such a reparameterization, however, a combined approach using an initial molecular mechanics investigation was found to be an efficient way to accurately characterize the ground-state geometry.

The excited-state lifetime of the homoleptic complex with the isopropylene bridged ligands was measured experimentally to be 50 times shorter at room temperature compared to the corresponding homoleptic complex with the methylene bridges. DFT calculations showed a difference between the two homoleptic complexes in terms of the lowest triplet excited-state potential energy surface. From the calculations, the changes in photophysical properties can be rationalized as being due to a structurally induced modification of the ligand field splitting of the d levels of the central metal ion.

An improved understanding of how various types of ligand modifications affect photophysical properties is important in the rational search for new metal complexes with potential applications in, for example, solar energy conversion systems. The results presented here demonstrate that photophysical properties, in particular excited-state lifetimes, can be strongly affected by ligand substitutions that essentially only change the coordination structure of the complex without influencing the electronic properties of the ligand. This suggests that it will be both interesting and important to consider how steric effects influence the solar energy conversion properties also of other complexes with flexible ligands. Combining photophysical measurements with emerging capabilities to investigate excited-state potential energy surfaces using first-principles quantum chemical calculations is seen to offer in-depth information about such effects.

Experimental Section

Synthesis. 2-[6-(2,2′-Bipyridyl)]-2-(2-pyridyl)propane (2). To a stirred solution of ligand **1** (0.22 g, 0.9 mmol), in 30 mL of dry THF, was added LDA (10 mL, 90 mM in THF, 0.9 mmol) at –30 °C. The solution was left under argon for 1 h. MeI (0.13 g, 0.91 mmol) was added, and the solution was warmed to reach room temperature over 2 h. Water was added and the mixture extracted with Et_2O. After the mixture was dried over Na_2SO_4 and solvent was removed, the crude product of the monomethylated ligand was treated with 1 equiv of LDA followed by MeI as described above. The final product was purified by column chromatography (silica gel, CH_2Cl_2/MeOH 16:1) (yield 0.12 g, 48%). ^{1}H NMR ($CDCl_3$, 25 °C): δ 1.88 (s, 6H), 7.14–7.20 (m, 2H), 7.24–7.31 (m, 2H), 7.62 (t, 1H), 7.72 (t, 1H), 7.80 (t, 1H), 8.23 (d, 1H), 8.43 (d, 1H), 8.62 (d, 1H), 8.66 (d, 1H).

$[Ru(2)_2][PF_6]_2$. A solution of ligand **2** (90 mg, 0.33 mmol), $Ru(DMSO)_4Cl_2$ (80 mg, 0.16 mmol), and silver trifluoromethanesulfonate (100 mg, 0.39 mmol) in H_2O/EtOH (1:2, 30 mL) was heated at reflux for 24 h. The reaction mixture was filtered and evaporated to dryness. The crude product was purified by column chromatography (silica gel, $CH_3CN/H_2O/KNO_3$ (sat), 90:5:1). After the solvent was evaporated, the product was dissolved in a small amount of CH_3CN/H_2O (2:1) and precipitated with NH_4PF_6 in water (62 mg, 40%). Crystals were grown from MeOH−Et_2O. ESI-MS (*m*/*z*): 797.20 (calcd $[M - PF_6^-]^+$, 797.15). ^{1}H NMR (CD_3CN, 25 °C): δ 1.82 (s, 6H), 2.36 (s, 6H), 6.2 (d, 2H), 6.82–6.92 (m, 4H), 7.71 (t, 4H), 7.82 (d, 2H), 7.95 (d, 2H), 8.20 (d, 2H), 8.31–8.39 (m, 4H), 8.48 (d, 2H).

$[Ru(ttpy)(2)][PF_6]_2$. $Ru(ttpy)(DMSO)Cl_2$ (62 mg, 0.11 mmol), ligand **2** (30 mg, 0.11 mmol), and silver trifluoromethanesulfonate (60 mg, 0.23 mmol) in H_2O−EtOH (1/2, 20 mL) was heated at reflux for 24 h. The reaction mixture was filtered and evaporated to dryness. The crude product was purified by column chromatography (silica gel, $CH_3CN/H_2O/KNO_3$ (sat), 90:5:1). After the solvent was evaporated, the product was dissolved in a small amount of CH_3CN/H_2O (2:1) and precipitated with NH_4PF_6 in water (36 mg, 34%). ESI-MS (*m*/*z*): 845.20 (calcd $[M - PF_6^-]^+$, 845.15). ^{1}H NMR (CD_3CN, 25 °C): δ 2.07 (s, 6H), 2.54 (s, 3H), 6.82 (t, 1H), 7.10 (t, 1H), 7.8–7.23 (m, 3H), 7.42 (d, 2H), 7.47 (d, 1H), 7.58–7.62 (m, 3H), 7.79 (t, 2H), 7.97 (t, 2H), 8.13 (d, 2H), 8.33–8.41 (m, 3H), 8.57–8.60 (m, 3H), 8.96 (s, 2H).

Mass Spectrometry. Experiments were done on a Bruker Daltonics BioAPEX-94e superconducting 9.4 T FTICR mass spectrometer (Bruker Daltonics, Billerica, MA) (ESI-FTICR MS).

Cyclic Voltammetry. Measurements were carried out in a three-compartment cell by using a glassy-carbon-disk working electrode, a platinum wire as the counter electrode, and a Ag/Ag^+ (10 mM $AgNO_3$ in CH_3CN) reference electrode. All potentials reported here are referenced vs the $Fc^{+/0}$ couple. The experiments were carried out in dry acetonitrile with 0.1 M tetrabutylammonium hexafluorophosphate as electrolyte.

UV–Vis Absorption. Spectra were measured on a Hewlett-Packard 8453 instrument or on a Varian Cary 50 UV–vis spectrophotometer in 1 × 1 cm quartz cuvettes.

Steady-State Emission. Measurements were performed on a SPEX-Fluorolog II fluorimeter and corrected for different detector sensitivities at different wavelengths. Spectra at 77 K were measured in a DN1704 variable-temperature liquid-nitrogen cryostat, and the temperature was set with an ITC601 intelligent temperature controller (Oxford Instruments). All emission measurements were carried out in a 1:4 (v/v) methanol/ethanol mixture in 1 × 1 cm quartz cuvettes. Emission quantum yields were estimated using $[Ru(bpy)_3]^{2+}$ as a reference compound, using the following relationship: $\Phi = (A/A_{ref}) \times (Abs_{ref}/Abs) \times \Phi_{ref}$, where A denotes the area of the emission spectrum and Abs the absorbance of the sample at the excitation wavelength (typically 460 nm). It was assumed that the refractive indices of the sample and the reference were the same, since they were measured in the same solvent.

Time-Resolved Emission. Measurements at 77 K were measured in a liquid-nitrogen-filled cold finger Dewar. Excitation light at 460 nm was produced with a frequency-tripled Q-switched Nd:YAG laser/OPO system from Quantel, producing <10 ns flashes. The emission was detected at a right angle with a monochromator and a P928-type PMT. The PMT output was recorded on a Phillips digital oscilloscope (2 G samples/s) and analyzed with a nonlinear least-squares algorithm with Applied Photophysics LKS60 software. At room temperature, excited-state lifetime measurements were performed with a time-correlated single-photon counting setup with 200 kHz laser pulses of 150 fs width generated in a regenerative amplified Ti:sapphire system from Coherent. The wavelength used for the experiments was 400 nm, obtained from doubling of the fundamental 800 nm light. The emission light was collected perpendicular to the incoming excitation light. A blue filter was used before the sample to remove remaining 800 nm light, and different red filters were used after the sample to remove excitation light. Emitted light was collected by a water-cooled Hammamatsu R38094-5 MCP PMT.

X-ray Diffraction. Single-crystal X-ray diffraction patterns were recorded with an Oxford Diffraction Excalibur diffractometer equipped with a sapphire-3 CCD on a Mo radiation source (λ = 0.710 73 Å) with ω scans at different φ values to fill the Ewald sphere. The sample–detector distance was 50 mm, and the maximum $2\theta \approx 63°$. Indexing, cell refinements, and integration of reflection intensities were performed with the Crysalis software.[21] Absorption correction was neglected, as it did not affect the model significantly; furthermore, the small size of the crystal and the low absorption coefficient made an absorption correction of minor importance. The structure was solved by direct methods using SHELXS97,[22] giving electron density maps where most of the non-hydrogen atoms could be resolved. The rest of the non-hydrogen atoms were located from difference electron density maps, and the structure model was refined with full-matrix least-squares calculations on F^2 using the program SHELXL97-2.[23] All non-hydrogen atoms were refined with anisotropic displacement parameters. The hydrogen atoms, which were placed at geometrically calculated positions and let ride on the atoms to which they were bonded, were given isotropic displacement parameters calculated as $\xi U_{eq.}$ for the nonhydrogen atoms with $\xi = 1.5$ for methyl hydrogens ($-CH_3$) and $\xi = 1.2$ for aromatic hydrogens. A packing diagram of Ru(**2**)$_2$ is provided in the Supporting Information. Note the large tunnels in the *c* direction of the structure. The structure was refined to a rather high *R* value (R1 $\approx$ 0.10), probably due to contributions from disordered solvent molecules present in the tunnels running along the *c* direction. The contribution from the disordered solvent of crystallization was partially removed by the use of the SQUEEZE procedure available in PLATON.[24] The resulting data set was used with SHELXL97-2, producing R1 = 0.0657 ($F^2 \geq 2\sigma(F^2)$). The Ru atom is placed at a special position (6h) in the space group $P\bar{3}1c$ (No. 163), giving the complex a 2-fold symmetry along the [120] direction.

Molecular Mechanics Calculations. These calculations were performed with MacroModel.[25,26] Initially, a molecular mechanics modeling study on the homoleptic complex [Ru(**2**)$_2$]$^{2+}$, using an MM3* force field specifically modified for ruthenium pyridyl complexes, was performed.[11]

Quantum Chemical Calculations. These calculations in the form of density functional theory (DFT) and time-dependent DFT (TD-DFT) calculations were performed using the B3LYP hybrid functional[27,28] together with the LANL2DZ effective core potentials and accompanying basis set.[29,30] The B3LYP/LANL2DZ computational method has previously been used successfully for highly similar systems.[16,17,31] All DFT calculations were performed using the Gaussian 03 program.[32] Full DFT geometry optimizations were performed to obtain ground-state conformers of [Ru(**2**)$_2$]$^{2+}$ using the MM3* structures as starting geometries. The most stable conformer was selected for further calculations. The geometries of the singlet (S_0) and triplet (^{3}MLCT and ^{3}MC) states of [Ru(**1**)$_2$]$^{2+}$ and [Ru(**2**)$_2$]$^{2+}$ were calculated by full geometry optimization. All three states for the two systems were optimized with a positive net charge (+2) and as a singlet state with restricted formalism in the case of S_0 and as triplet states with unrestricted formalism for ^{3}MLCT and ^{3}MC. The geometry optimizations were restricted to C_2 symmetry. For the S_0 state, 30 vertical singlet excitations and 12 vertical triplet excitations were calculated by TD-B3LYP/LANL2DZ. The energies of the S_0 surface corresponding to the ^{3}MLCT and ^{3}MC geometries were calculated by single-point calculations.

Acknowledgment. This work was supported by the Swedish Energy Agency, the Swedish Research Council (VR), the Göran Gustafsson Foundation, and the Knut and Alice Wallenberg Foundation. The Swedish National Supercomputer Centre (NSC) and UPPMAX are acknowledged for grants of computer time.

Supporting Information Available: An X-ray diffraction packing diagram for [Ru(**2**)$_2$]$^{2+}$ and a table giving calculated electronic transitions from the ground states of [Ru(**1**)$_2$]$^{2+}$ and [Ru(**2**)$_2$]$^{2+}$. This material is available free of charge via the Internet at http://pubs.acs.org.

IC7019457

(21) *Xcalibur CCD System, CrysAlis Software System, Version 1.170*; Oxford Diffraction Ltd., Oxford, U.K., 2003.
(22) Sheldrick, G. M. *Acta Crystallogr., Sect. A* **1990**, *A46*, 467.
(23) Sheldrick, G. M. *SHELXL97-2, Computer Program for the Refinement of Crystal Structures*; University of Göttingen, Göttingen, Germany, 1997.
(24) Spek, A. L. *J. Appl. Crystallogr.* **2003**, *36*, 7.
(25) *MacroModel, version 7.2*; Schrödinger Inc., Portland, OR; http://www.schrodinger.com.
(26) Mohamadi, F.; Richards, N. G. J.; Guida, W. C.; Liskamp, R.; Lipton, M.; Caulfield, C.; Chang, G.; Hendrickson, T.; Still, W. C. *J. Comput. Chem.* **1990**, *11*, 440.
(27) Becke, A. D. *J. Chem. Phys.* **1993**, *98*, 5648.
(28) Lee, C. T.; Yang, W. T.; Parr, R. G. *Phys. Rev. B* **1998**, *37*, 785.
(29) (a) Dunning, T. H., Jr.; Hay, P. J. In *Modern Theoretical Chemistry*; Schaefer, H. F., III, Ed.; Plenum: New York, 1976; Vol. *3*, pp 1–28. (b) Hay, P. J.; Wadt, W. R. *J. Chem. Phys.* **1985**, *82*, 299.
(30) Hay, P. J.; Wadt, W. R. *J. Chem. Phys.* **1985**, *82*, 299.
(31) Guillemoles, J. F.; Barone, V.; Joubert, L.; Adamo, C. *J. Phys. Chem. A* **2002**, *106*, 11354.
(32) Frisch, M. J.; Trucks, G. W.; Schlegel, H. B.; Scuseria, G. E.; Robb, M. A.; Cheeseman, J. R.; Montgomery, J. A., Jr.; Vreven, T.; Kudin, K. N.; Burant, J. C.; Millam, J. M.; Iyengar, S. S.; Tomasi, J.; Barone, V.; Mennucci, B.; Cossi, M.; Scalmani, G.; Rega, N.; Petersson, G. A.; Nakatsuji, H.; Hada, M.; Ehara, M.; Toyota, K.; Fukuda, R.; Hasegawa, J.; Ishida, M.; Nakajima, T.; Honda, Y.; Kitao, O.; Nakai, H.; Klene, M.; Li, X.; Knox, J. E.; Hratchian, H. P.; Cross, J. B.; Bakken, V.; Adamo, C.; Jaramillo, J.; Gomperts, R.; Stratmann, R. E.; Yazyev, O.; Austin, A. J.; Cammi, R.; Pomelli, C.; Ochterski, J. W.; Ayala, P. Y.; Morokuma, K.; Voth, G. A.; Salvador, P.; Dannenberg, J. J.; Zakrzewski, V. G.; Dapprich, S.; Daniels, A. D.; Strain, M. C.; Farkas, O.; Malick, D. K.; Rabuck, A. D.; Zaghavachari, K.; Foresman, J. B.; Ortiz, J. V.; Cui, Q.; Baboul, A. G.; Clifford, S.; Cioslowski, J.; Stefanov, B. B.; Liu, G.; Liashenko, A.; Piskorz, P.; Komaromi, I.; Martin, R. L.; Fox, D. J.; Keith, T.; Al-Laham, M. A.; Peng, C. Y.; Nanayakkara, A.; Challacombe, M.; Gill, P. M. W.; Johnson, B.; Chen, W.; Wong, M. W.; Gonzalez, C.; Pople, J. A. *Gaussian 03, Revision B.05*; Gaussian, Inc., Wallingford, CT, 2003.